Wind Energy

WIND ENERGY
*Wind Energ.* 2016; **19**:803–824
Published online 16 June 2015 in Wiley Online Library (wileyonlinelibrary.com). DOI: 10.1002/we.1866

RESEARCH ARTICLE

# Influence of inflow conditions on turbine loading and wake structures predicted by large eddy simulations using exact geometry

Nina Zhou[1], Jun Chen[1], Douglas E. Adams[2] and Sanford Fleeter[1]

[1] School of Mechanical Engineering, Purdue University, West Lafayette, Indiana, 47907, USA
[2] School of Engineering, Vanderbilt University, Nashville, Tennessee 37235, USA

## ABSTRACT

A large eddy simulation was performed on an National Renewable Energy Laboratory (NREL) phase VI wind turbine (10 m diameter), using the exact blade geometry, to determine the influence of different inflow conditions on the aerodynamic loadings and the near wake characteristics. The effects of the three inflow conditions, uniform inflow, linear wind shear and linear wind shear with turbulence, are investigated. Wind shear causes periodic variations in power and aerodynamic loading with an additional force component exerted along the lateral direction. Significant separation occurs in the high wind region on the suction side of the blades, resulting in unstable loading in off-design inflow conditions. Because of the shear effect between the near-blade tip vortex and ambient flow, the strong vortex core in the helical structure dissipates and transforms into a continuous vorticity sheet when $x/D > 1.5$. The combination of inflow turbulence and wind shear enhances the turbulence generation mechanism in the near wake, where energy is withdrawn from large wake structures and converted into energy of small-scale structures. Copyright © 2015 John Wiley & Sons, Ltd.

**KEYWORDS**
large eddy simulation; wake characteristics; aerodynamic loadings; wind shear; turbulence intensity

**Correspondence**
J. Chen, Mechanical Engineering, Purdue University, West Lafayette, Indiana, 47907, USA.
E-mail: junchen@purdue.edu

Received 17 April 2015; Accepted 1 May 2015

## NOMENCLATURE

| | |
|---|---|
| $\alpha$ | wind shear exponent |
| $\delta t$ | time step in simulation |
| $\Delta$ | characteristic scale of the filtering kernel |
| $\delta\theta$ | rotation angle turbine blade sweeps per time step |
| $\delta_{ij}$ | Kronecker delta |
| $\kappa$ | von Karman constant |
| $\langle\cdot\rangle$ | averaging operation |
| $\tilde{\mathbf{u}}'$ | velocity fluctuations, $\tilde{\mathbf{u}}' \equiv (\tilde{u}', \tilde{v}', \tilde{w}')$ |
| $\mathbf{u}$ | flow velocity, $\mathbf{u} \equiv (u, v, w) \equiv (u_1, u_2, u_3)$ |
| $\mathbf{x}$ | location vector, $\mathbf{x} \equiv (x, y, z) \equiv (x_1, x_2, x_3)$ |
| $\mu_t$ | sub-grid scale eddy viscosity |
| $\nu$ | kinematic viscosity of fluid |
| $\omega_r$ | vorticity vector in spanwise direction |
| $\omega_x$ | non-dimensional streamwise vorticity |
| $\rho$ | density of air |
| $\tau_{ij}$ | sub-grid scale (sgs) stress |
| $\tilde{S}$ | magnitude of resolved strain rate |
| $\tilde{S}_{ij}$ | resolved strain rate tensor |

| | |
|---|---|
| $A$ | turbine blade swept area |
| $c$ | chord length of wind turbine blade |
| $C_p$ | pressure coefficient |
| $C_s$ | Smagorinsky coefficient |
| $C_w$ | power coefficient |
| $C_{F_x}$ | axial force coefficient |
| $C_{F_y}$ | lateral force coefficient |
| $C_{F_z}$ | vertical force coefficient |
| $D$ | wind turbine diameter |
| $e$ | turbulent kinetic energy |
| $G_\Delta$ | filtering kernel |
| $I_u$ | streamwise turbulence intensity |
| $\mathcal{P}_{uv}$, $\mathcal{P}_{uw}$ | turbulence production components |
| $R$ | wind turbine radius |
| $r$ | radius coordinate |
| $rms$ | root mean square |
| $u_\tau$ | wall friction velocity |
| $U_o$ | free stream velocity |
| $U_{\text{hub}}$ | velocity at hub height |
| $U_{rel}$ | relative velocity of wind |
| $y^+$ | non-dimensional wall distance for a wall-bounded flow |

## 1. INTRODUCTION

Wind energy is among the mature techniques for large-scale renewable energy production with promising future commercial prospects.[1,2] Optimal design of wind turbines maximizes the energy harvest under certain ideal design conditions. However, their actual performance is greatly affected by the temporal and spatial wind characteristics. In utility-scale wind farms where arrays of wind turbines are installed, the wind profile and turbulence level in the atmospheric boundary layer (ABL) influence the performances of leading wind turbines, whereas the wake of the upstream turbines acts as disturbed incoming flow for the downstream wind turbines. These off-design inflow conditions lead to significant production losses and escalated fatigue loads. For example, a 10% reduction in power output was reported for three turbines separated by $7D$ ($D$ is the rotor diameter)[3] and a power deficit up to 45% in a large offshore wind farm.[4] Full-wake conditions increase downstream turbine loading by as much as 80%.[5] The cyclic loading can trigger crack growth of turbine components, ultimately resulting in structural failure and significantly reducing the life duty of wind turbine. Optimal design and control of utility-scale farms with maximized energy harvest and minimized maintenance costs require a detailed understanding of the effects of inflow conditions, in particular the mean wind profile and turbulence characteristics on turbine wakes.

The wake shed from a wind turbine is divided into near wake and far wake. Near wake is contained within approximately one rotor diameter downstream of the rotor, while the far wake is further downstream.[6] To characterize wind turbine wakes, field measurements have been made to determine the change of wind direction and turbulence level, and laboratory experiments have been conducted in wind tunnels under controlled conditions (e.g., previous studies[6–15]). These experiments developed a general picture of wind turbine wakes but were fundamentally limited since (i) they were limited to small scales and low Reynolds numbers, (ii) they were not conducted in a turbulent sheared flow as in realistic operation conditions, and (iii) the available measurement techniques could not resolve the complete temporal–spatial features of the wake. In addition, the currently available experimental datasets are insufficient for validating model development and numerical simulations of large-scale wind turbines, especially in the wake region.

Computational fluid dynamics provides an alternative tool to study detailed interactions between rotating turbines with realistic inflow conditions. In a Reynolds-averaged Navier–Stokes (RANS) simulation, a specific flow variable $f(\mathbf{x},t)$ (velocity, pressure, etc.) is decomposed into a time-averaged mean variable $\langle f(\mathbf{x})\rangle$ and a corresponding fluctuating variable $f'(\mathbf{x},t) = f(\mathbf{x},t) - \langle f(\mathbf{x})\rangle$, where $\langle\cdot\rangle$ represents the averaging operation. The mean variables are solved from RANS equations with the help of turbulence models. RANS methods have been widely used to study wind turbines[16–22] in which correct prescription of the turbulent inflow was crucial for valid predictions. Another simulation technique, large eddy simulation (LES), decomposes the flow variable $f(\mathbf{x},t)$ into a resolved part $\tilde{f}(\mathbf{x},t)$, depicting the large-scale motions, and a sub-grid scale (SGS) part $f^{\text{sgs}}(\mathbf{x},t) = f(\mathbf{x},t) - \tilde{f}(\mathbf{x},t)$, where $\tilde{\cdot}$ represents a spatial filtering operation. The resolved parameters are solved from the filtered Navier–Stokes equations by employing SGS models to describe the unresolved motions. LES is able to simulate the unsteady, anisotropic turbulent flows dominated by large-scale structures and turbulent


*Wind Energ.* 2016; **19**:803–824 © 2015 John Wiley & Sons, Ltd.
DOI: 10.1002/we

mixing.[23] The results of simulating wind turbine wakes using the RANS method (with standard $k-\epsilon$ model) and the LES method are compared by Stovall *et al.*[24] The comparison showed that LES captures the wake recovery more accurately than RANS. Although LES is more computationally expensive, the rapid increase in computational capacities has enabled its application in wind energy research.[25–34] Jimenez *et al.*[25–27] applied the LES method along with the uniformly loaded actuator disk technique to study the wind turbine wake. Troldborg *et al.*[28] reported a series of numerical simulations of wind turbine wakes under uniform inflow with varying tip-speed ratios using an actuator line technique coupled with LES. Porté-Agel *et al.*[29] adopted a Lagrangian scale-dependent dynamic SGS model in LES along with the actuator disk and actuator line methods to study turbine wakes in a turbulent boundary layer. They further extended the simulation to a wind farm to analyze the velocity field and turbulence levels in the wake region, as well as power reduction of downstream wind turbines. Lu *et al.*[30] combined LES with the actuator disk method to simulate the interaction of a stably stratified ABL with wind farm. Characterization of wake behavior was conducted by the vorticity-based mixed-scale SGS model with the actuator line method.[28,35]

Even with the aforementioned efforts, few publications bring insights into the wind turbine performance and wake characteristics under varying inflow conditions. The two turbine simulations by Troldborg *et al*[36] employed different levels of ambient turbulence intensity, representing laminar, offshore and onshore conditions and identified the presence of turbulence that caused wake breakdown and early formation of fully developed turbulence. The wake structures and wind turbine performance under uniform steady inflow, steady vertical wind shear and transient extreme wind shear conditions are studied by Sezer-Uzol and Uzol[37] by applying a three-dimensional unsteady vortex-panel method. It was determined that the wind shear resulted in asymmetric and non-periodic wake structure and high levels of fluctuations in power. This method allows a relatively fast simulation, but, due to the assumption of inviscid flow, its prediction lacks the capability of capturing the complex flow physics, such as flow separation around the blade surface.

Furthermore, wind farm control models can be developed to maximize the energy harvest and to minimize the operation cost of the wind turbine clusters. To achieve these benefits, the existing wake and aerodynamic models must be improved based on an in-depth understanding of the wind turbine performance and wake characteristics under various inflow conditions. The motivation of this study is to gain a detailed understanding of how wind shear and inflow turbulence affect wake structures, turbine blade loading and energy capture. LES is applied to study the flow field around a rotating NREL phase VI wind turbine (two-blade, $D \sim 10$ m), using exact blade geometry. Three cases with varying inflow conditions are studied. The results are validated using measurement data, and then a systematic wake characterization is conducted. This paper is organized as follows. Details of the numerical routine are presented in Section 2. The three cases with three different inflow conditions are described in Section 3. Results and discussions are given in Section 4 followed by the conclusions in Section 5.

## 2. METHODOLOGY

### 2.1. Governing equations of LES and SGS model

In LES, a low-pass filtering operation is applied to a flow variable $f(\mathbf{x}, t)$ to obtain a resolved part

$$\tilde{f}(\mathbf{x}, t) = \int G_\Delta(\mathbf{x}', \mathbf{x}) f(\mathbf{x} - \mathbf{x}', t) d\mathbf{x}' \tag{1}$$

and a SGS part

$$\tilde{f}^{\mathrm{sgs}}(\mathbf{x}, t) = f(\mathbf{x}, t) - \tilde{f}(\mathbf{x}, t) \tag{2}$$

where $G_\Delta$ is a filtering kernel with a characteristic scale $\Delta$. With an assumption of incompressible flow, the resolved velocity ($\tilde{u}_i$) and pressure ($\tilde{p}$) fields can be solved from the filtered Navier–Stokes equations

$$\frac{\partial \tilde{u}_i}{\partial x_i} = 0, \tag{3}$$

$$\frac{\partial \tilde{u}_i}{\partial t} + \tilde{u}_j \frac{\partial \tilde{u}_i}{\partial x_j} = -\frac{1}{\rho}\frac{\partial \tilde{p}}{\partial x_i} + \nu \frac{\partial^2 \tilde{u}_i}{\partial x_j \partial x_j} - \frac{1}{\rho}\frac{\partial \tau_{ij}}{\partial x_j}. \tag{4}$$

Here, $\tau_{ij}$ is the SGS stress

$$\tau_{ij} = \widetilde{u_i u_j} - \tilde{u}_i \tilde{u}_j, \tag{5}$$

which must be modeled in order to close Equations 3 and 4. The most popular SGS models are the eddy viscosity type, relating the deviatoric part of SGS stress with the resolved strain

$$\tau_{ij} - \frac{1}{3}\tau_{kk}\delta_{ij} = -2\mu_t \tilde{S}_{ij} \tag{6}$$

where $\mu_t$ is the SGS eddy viscosity. $\tilde{S}_{ij}$ is the resolved strain rate tensor given by

$$\tilde{S}_{ij} = \frac{1}{2}\left(\frac{\partial \tilde{u}_i}{\partial x_j} + \frac{\partial \tilde{u}_j}{\partial x_i}\right). \tag{7}$$

Smagorinsky[38] further modeled the eddy viscosity using the mixing length hypothesis

$$\mu_t = \ell_s^2 \tilde{S}, \tag{8}$$

where $\tilde{S} = \sqrt{2\tilde{S}_{ij}\tilde{S}_{ij}}$. Furthermore, for regions close to solid surfaces, $\ell_s$ is determined by

$$\ell_s = \min(\kappa d, C_s \Delta) \tag{9}$$

where $\kappa$ is the von Karman constant, $d$ the distance to the closest wall, and $C_s$ the Smagorinsky coefficient. In the present study, a constant value of Smagorinsky coefficient, $C_s = 0.1$, is adopted. This value is empirically tuned for wall-modeled LES.[39]

## 2.2. Computational domain and NREL phase VI wind turbine

Researchers performed an experimental study of an NREL phase VI wind turbine in NASA Ames 24.4 m × 36.6 m wind tunnel. The details of the experiments and results reported by Hand *et al.*[40] and Simms *et al.*[41] help to validate computational fluid dynamics predictions. The same condition was adopted for model validation in this study. The computational domain in this study is illustrated in Figure 1, with a length (streamwise) $L_x = 55.3$ m, height $L_z = 24.4$ m and width $L_y = 36.6$ m, identical to the test section of the Ames wind tunnel. The stall-regulated NREL phase VI wind turbine has two twisted and taped blades, and each blade is constructed by a series of S809 airfoil profiles. The blades twist from a maximum angle of 20.04° at the root to a minimum of −2.15° at the tip. The rotor is of diameter $D = 10.06$ m, pitch angle 3.5° and yaw angle 0°. The hub of the wind turbine is placed 12.2 m above the ground, 2$D$ from the inflow boundary and 3.5 $D$ from the outlet. The origin of coordinate system is set at the hub center, with $x$ pointing to streamwise direction and $z$ antiparallel to gravity (vertically upward). In the simulation, both the tower and nacelle are omitted from the computational domain. Consequently, flow interactions between the blades, tower and nacelle are not considered.

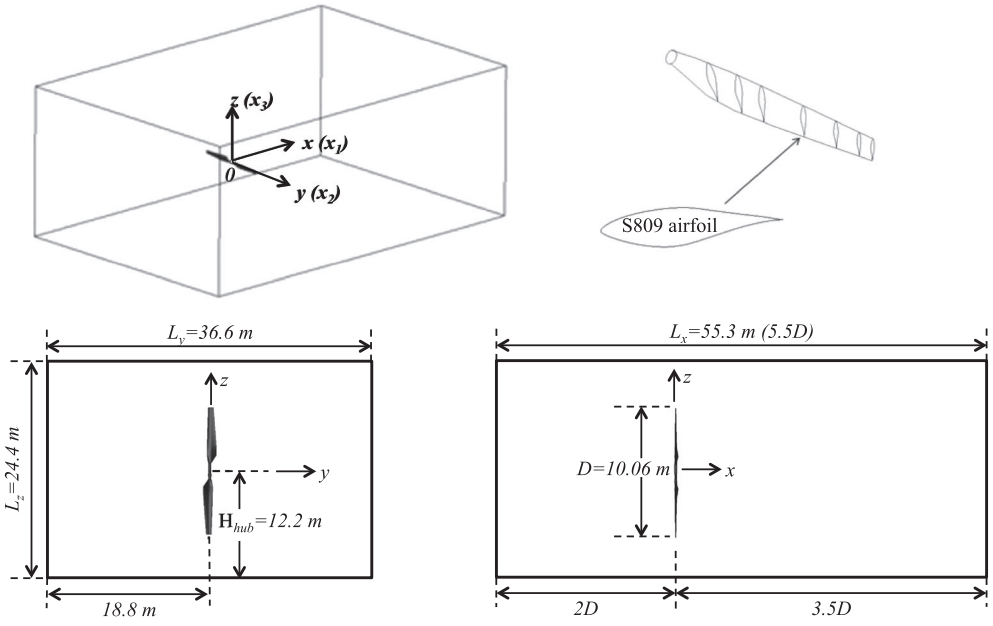


**Figure 1.** Schematics of the computational domain.

### 2.3. Computational mesh and near-wall treatment

A multi-block method is used to generate the computation mesh including the sliding mesh zone and the stationary mesh zone. As shown in Figure 2(a), hexahedral grids are generated surrounding the wind turbine blades. The first layer of grid is 1 mm away from the blade surface to ensure that $y^+$ is in the range of 30–300, for valid implementation of a wall function ($y^+$ is the non-dimensional distance measured from the wall, defined in the succeeding text). A total of 20 layers of grids are sequentially attached to the blade surface with an increase ratio of 1.1 along surface normal direction. There are 70 mesh points distributed along the chordwise direction at each section of the blades, and grids are more concentrated at the leading and trailing edges. A total of 150 mesh points are distributed in the spanwise direction of each of the blades. In

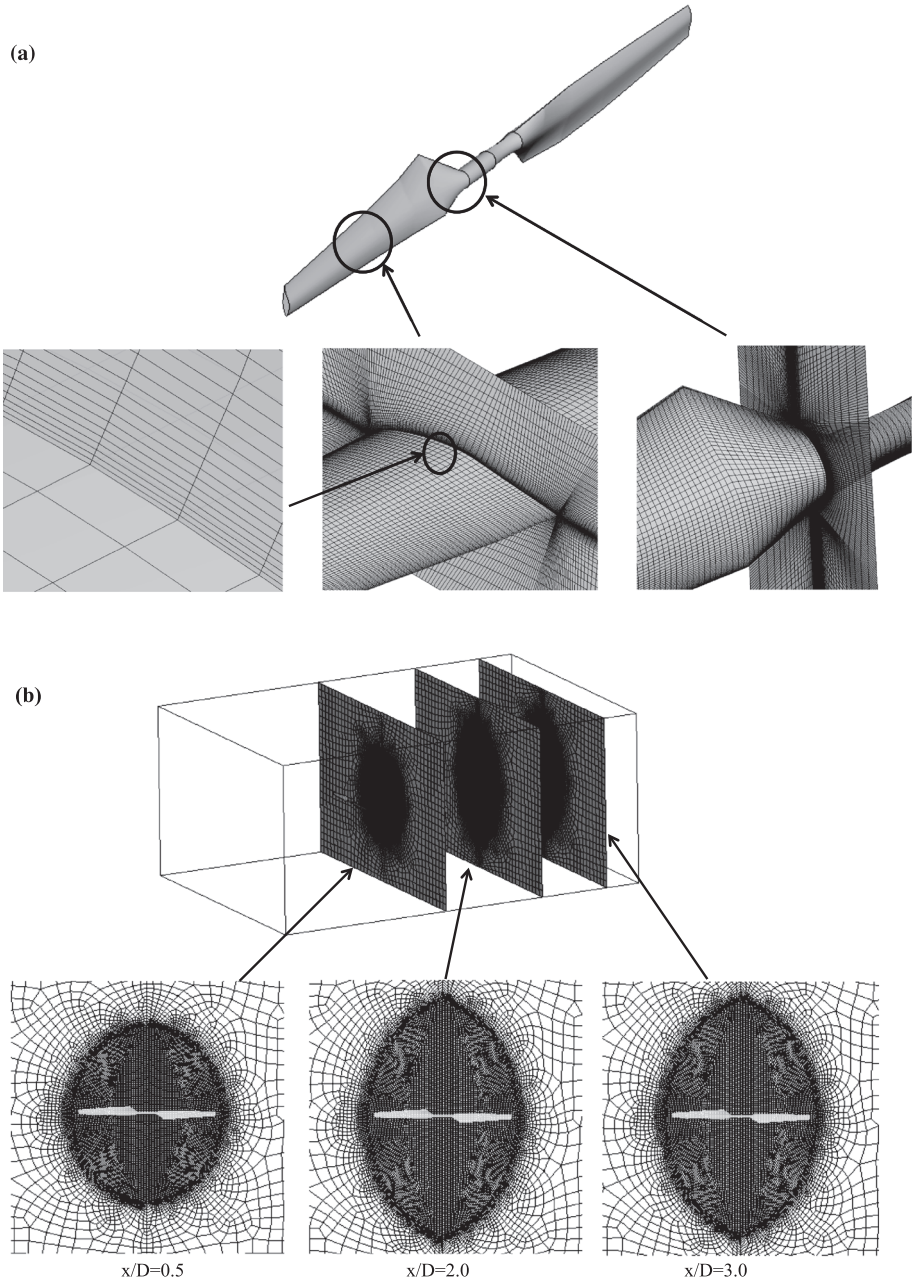


**Figure 2.** Schematics of computation mesh. (a) Grid distribution around wind turbine blade. (b) Details of grid distribution at different downstream locations.

order to better capture the wake characteristics, a uniform mesh spacing is implemented in $x$-direction. Figure 2(b) shows the mesh distribution in several downstream locations in $y$-$z$-plane. The total number of grids is $5.23 \times 10^6$. In the present study, the wall function[42] adopted to model the near-wall physics is

$$u^+(y^+) = \begin{cases} y^+, & if\ y^+ < 11.8 \\ 8.3(y^+)^{1/7}, & if\ y^+ > 11.8 \end{cases} \tag{10}$$

where $u^+ = u/u_\tau$. Here, $u$ is the velocity component parallel to the wall surface, $u_\tau$ is the friction velocity and

$$y^+ = u_\tau y'/\nu \tag{11}$$

where $y'$ is the wall normal distance measured from the cell centers.

### 2.4. Sliding mesh approach and numerical solver

A sliding mesh approach is employed to capture the unsteady flow field around the rotating blades. The sliding mesh zone and stationary zone are bounded by the interfaces with disaligned mesh once the rotation takes place. Information of the two mesh zones is interchanged through the interface mesh, which is recalculated after each time step. The numerical solver in ANSYS FLUENT 14.0 is employed in the present LES study, while a user-defined function is implemented to prescribe the inflow conditions. The convection terms in all transport equations are discretized using the bounded central differencing schemes to avoid damping out the energy of resolved eddies. The transient terms are discretized using the first-order implicit scheme. A RANS simulation with a time step $\delta t = 0.00579$ s (corresponding to a rotation angle $\delta\theta = 2.5°$) is first carried out to set up the initial flow field. After one revolution, LES is activated. A total of 30 revolutions are computed with a relatively large time step to wash out the initial flow field established by RANS. Another time step of $\delta t = 0.00023$ s ($\delta\theta = 0.1°$) is then chosen to better predict flow variables in the boundary layer, e.g., the pressure distribution. The drag forces of the blades and the velocity evolution at different locations in the domain are monitored during the entire simulation period. In all the cases, the simulation lasts for at least 17 revolutions with the small time step to collect sufficient sampling data. A total of 61,200 snapshots are used to achieve convergence of the statistical analysis.

## 3. SIMULATION CONDITIONS

Three different sets of inflow conditions are simulated in the present study

(1) Baseline case. Identical inflow conditions as those used in experiments.[40,41] A uniform velocity profile ($U_o = 7.0$ m s$^{-1}$) with 0° yaw angle is prescribed at the inlet. As in wind tunnel tests, the turbulence level at the inlet is small, so a laminar wind profile is adopted. The rotor rotates at 72 rpm, giving a tip-speed ratio of 5.4. The Reynolds number

$$Re = \frac{U_{\text{rel}} \cdot c}{\nu} \tag{12}$$

is in the order of $10^6$, where $U_{\text{rel}}$ is the relative wind velocity, $c$ the chord length of turbine blade and $\nu$ the kinematic viscosity of air. Atmosphere pressure is specified at the outlet. The top, bottom, side surfaces and the blade surfaces are set to no-slip conditions with zero velocities, identical to the test sections in the experiments.

(2) Wind shear case. Linear wind shear profile with negligible turbulence. The mean wind profile in ABL is modeled by a power law

$$\langle u \rangle(z') = U_{\text{hub}} \cdot \left(\frac{z'}{z'_{\text{hub}}}\right)^{\alpha}, \tag{13}$$

where $U_{\text{hub}}$ is the mean wind velocity at hub height ($z' = z'_{\text{hub}}$, the ground is at $z' = 0$). The wind shear exponent $\alpha$ is 0.07 and 0.43 for the ice terrain and woodlands, respectively.[43] In this study, the wind profile in the rotor-swept area (not starting from ground) is of interest. A linear wind profile in this region is approximated by choosing $\alpha = 0.35$ and a hub velocity $U_{\text{hub}} = 7.0$ m s$^{-1}$, as shown in Figure 3. Consequently, the wind profile applied on the inlet of the computation domain is

$$\langle u \rangle(z) = 5.1 \cdot \left(\frac{z}{24.4} + 0.5\right) + 4.45, \tag{14}$$

where the units for $\langle u \rangle$ and $z$ are meter per second and meter, respectively. This linear wind profile yields the same mass flow rate as the baseline case. Comparing results from this case with results from the baseline case may highlight the influence of wind shear. The top and bottom surfaces of the computation domain have constant velocities consistent


*Wind Energ.* 2016; **19**:803–824 © 2015 John Wiley & Sons, Ltd.
DOI: 10.1002/we

with the wind profile. The outlet boundary conditions, rotation of the blades and the side surfaces and blade surfaces are the same as the baseline case.

(3) Turbulent shear case. The same wind shear profile as the second case with added turbulence. A three-dimensional velocity fluctuation is introduced using the spectral synthesizer method.[44,45]
Simulated turbulence intensity (streamwise component, $I_u = u_{\mathrm{rms}}/U_{\mathrm{hub}}$) profiles with different roughness lengths ($z_0 = 0.00005 - 0.5$ m) were reported by Wu and Porté-Agel,[46] ranging from 4% to 14% at hub height. In the work of Christakos *et al.*,[47] distributions of $I_u$ at 100 m above sea level (asl) (typical $z$-level of nacelle height of the state-of-the-art wind turbines) for different classes of wind speed were plotted based on 4 year offshore Lidar measurements, where $I_u$ is about 8% with wind speed ranging from 5 to 10 m s$^{-1}$. To match these experimental observations, $I_u = 8\%$ was selected for this simulation. The boundary conditions other than the inlet conditions are equivalent to case 2.

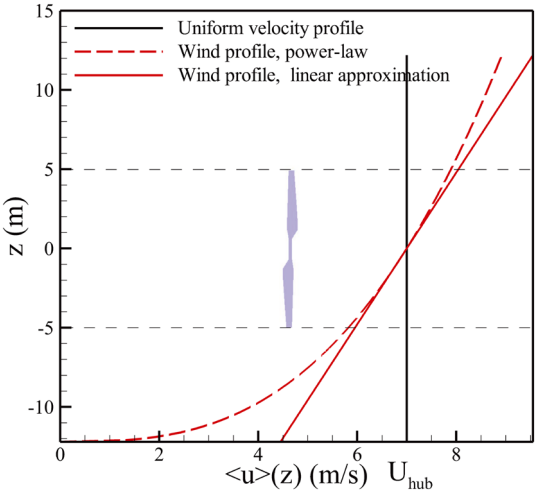


**Figure 3.** Different inflow wind profiles: uniform profile, power-law profile and approximated linear profile.

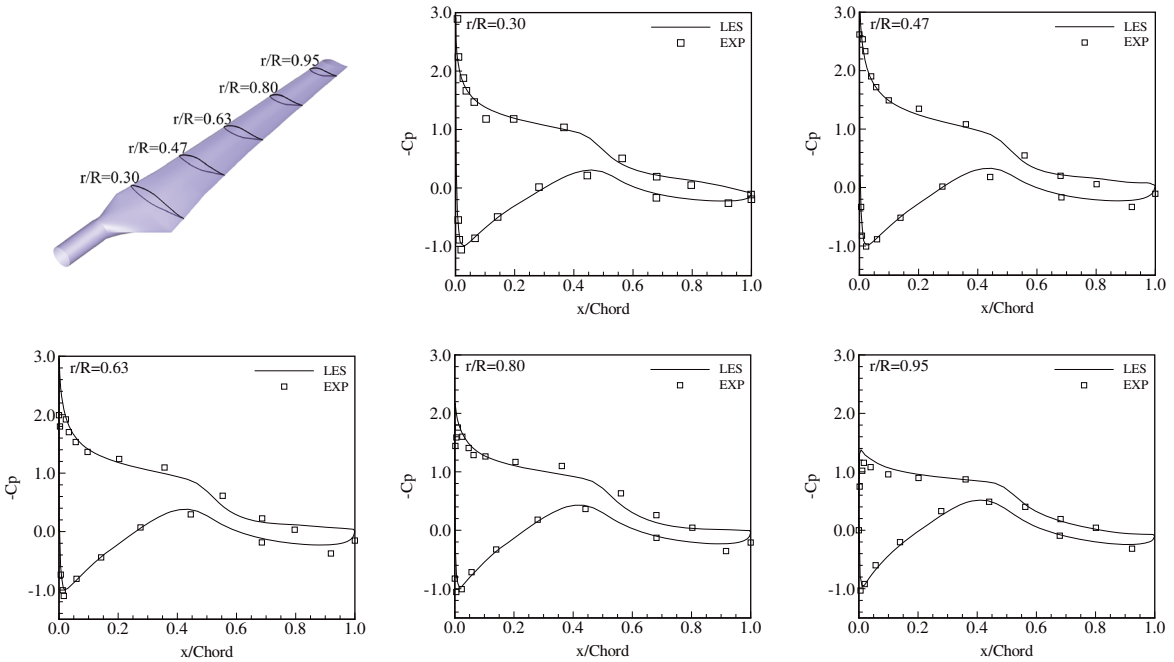


**Figure 4.** Comparison of mean pressure coefficients predicted by LES and experimental results at different spanwise sections.

# 4. RESULTS AND DISCUSSION

## 4.1. Validation of LES results of baseline case

The pressure distribution along the blade at five spanwise sections was measured in wind tunnel experiments.[40,41] Figure 4 compares the time-averaged LES results of the pressure coefficient $C_p$ with the experimental results at sections of $r/R = 0.3, 0.47, 0.63, 0.8$ and $0.95$. The LES results agree well with the measured data. $C_p$ on the pressure side matches well

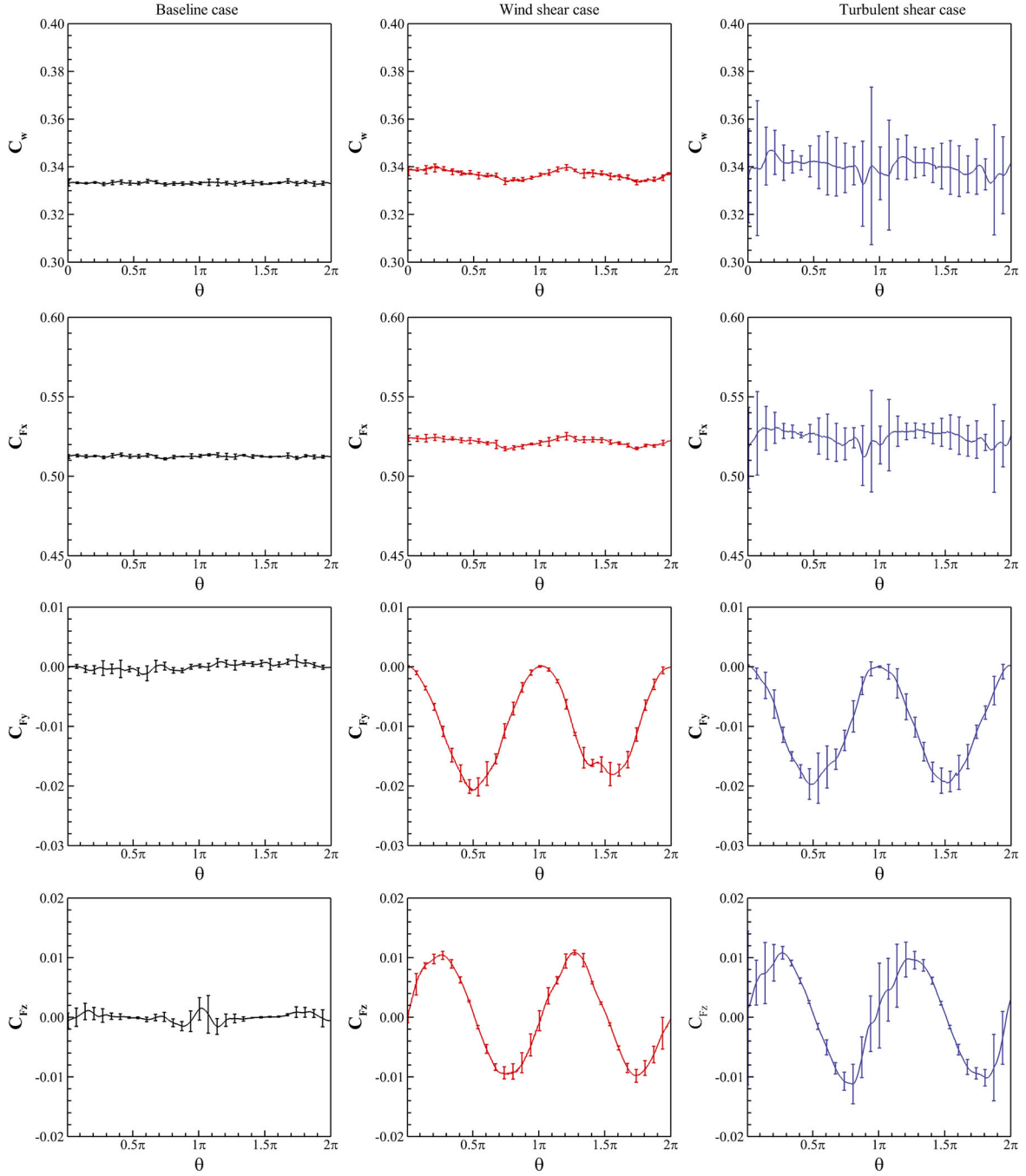


**Figure 5.** Comparison of phase-averaged output power coefficients and aerodynamic load coefficients under three flow conditions: (left) baseline case, (middle) wind shear case and (right) turbulent shear case. Error bars give the corresponding rms values.


*Wind Energ.* 2016; **19**:803–824 © 2015 John Wiley & Sons, Ltd.
DOI: 10.1002/we

with the measured data, while a slight discrepancy is observed at $x/c = 0$ on the suction side when $r/R$ is 0.63, 0.80 or 0.95. A similar mismatch of $C_p$ at the leading edge is also reported by Mo *et al.*[31] at $r/R = 0.80$ and 0.95. These under-predictions are likely due to the occurrence of tip vortices, and the averaging effect associated with the finite size of pressure ports used for the measurements. The LES routine presented here is able to effectively predict the aerodynamic loadings applied on the turbine blades. On the other hand, the wake characteristics are related to the momentum change in the streamwise direction,[48] which causes pressure differences on turbine blades. Since the wake measurement data are not available, the accurate prediction of $C_p$ is also considered as a validation for predicting wake characteristics and turbulent wake characteristics under varying inflow conditions.

## 4.2. Power production and aerodynamic loads

The torque and forces applied on the wind turbine are computed by integrating the pressure distribution on the blade surfaces. In order to identify the effects of the inflow conditions on wind turbine performance and loading status, we computed the phase-averaged output power coefficient

$$C_w = \frac{\text{Power}}{\frac{1}{2}\rho A U_{hub}^3} \tag{15}$$

and the force coefficients (in $x$-direction, $y$-direction and $z$-direction)

$$\left(C_{F_x}, C_{F_y}, C_{F_z}\right) = \frac{(F_x, F_y, F_z)}{\frac{1}{2}\rho A U_{hub}^2} \tag{16}$$

as shown in Figure 5 under three inflow conditions. For the baseline case, $C_w$ is relatively stable and has an average value of 0.333, with a 5.9% difference when compared with the measured power coefficient of 0.354. In the wind shear case, an oscillation of the power coefficient is observed, with an average value of 0.337. Significant fluctuations of $C_w$, indicated by the rms values, are observed for the turbulent shear case, with the largest average value of 0.341 among all three cases. (The increase in the mean value is not significant). It is obvious that the turbulent wind shear flow condition results in the

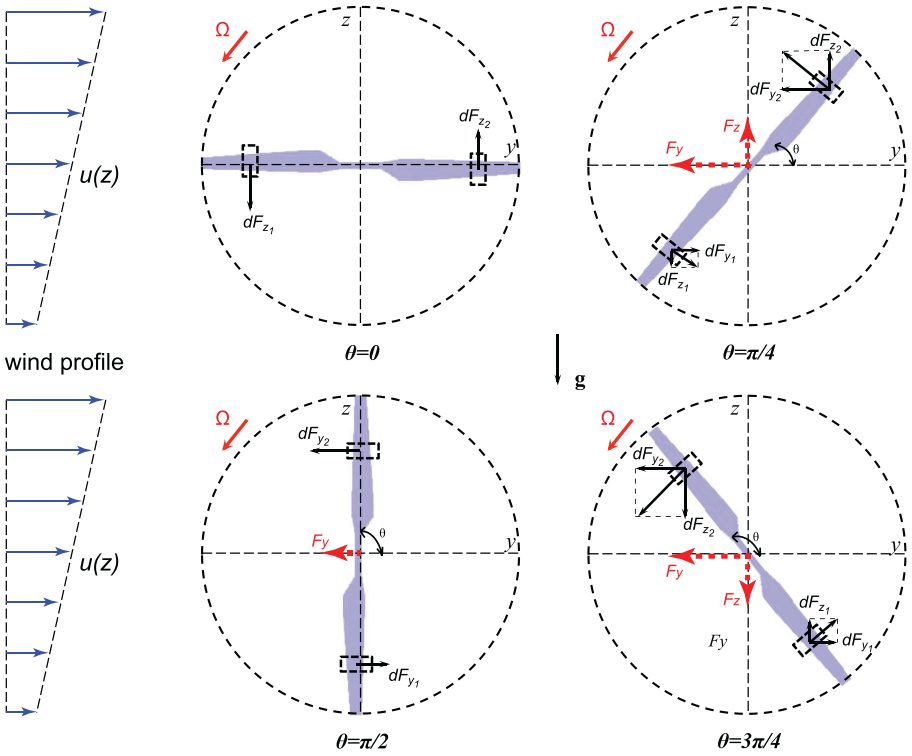


**Figure 6.** Schematics of the force analysis.

most unstable power production, and peak fluctuation can reach about 22% of the average value, estimated by twice the rms values.

Quantifying the effect of the inflow conditions on the change of aerodynamic loadings on wind turbines is a direct index of the fatigue loading applied on the wind turbine. The phase-averaged force coefficients (three components) are also illustrated in Figure 5. One is reminded that $\theta = 0$ is the phase when the turbine blades are in horizontal positions. The average values of $C_{F_x}$ (streamwise force coefficient) for the three cases are 0.513, 0.522 and 0.525, respectively. Similar to the behavior of $C_{\mathrm{w}}$, the wind shear case has a peak rms of $\pm 7.5\%$ at phase $\theta{=}\pi$. $C_{F_y}$ and $C_{F_z}$ are about zero for the baseline case, indicating an idealized loading status. However, in the wind shear case and turbulent shear case, $C_{F_y}$ and $C_{F_z}$ display a periodic pattern with an amplitude of 0.01 for both cases, which is caused by the phase difference between the applied wind shear (along $z$-direction) and two rotating blades. In addition to the periodic variation, the turbulent shear case yields more random fluctuation, indicated by the error bars with maximum rms values of 0.004 ($C_{F_y}$) and 0.013 ($C_{F_z}$). Most importantly, $C_{F_y}$ periodically oscillates around a similar direct current (DC) offset (mean value of periodic pattern) of $\simeq -0.01$ for both wind shear and turbulent shear cases. This offset suggests that in the presence of wind shear in the vertical direction (as in ABL), there is a non-zero lateral load (in $y$-direction) on the wind turbine. To explain this phenomenon, Figure 6 shows the schematic of the force components in $y$–$z$-plane on two symmetric sections on both turbine blades when wind shear is present. At $\theta = 0$, only non-zero $F_z$'s exist, and the resultant force components are zero due to symmetry. At $\theta = \pi/4$, the resultant force component in $y$-direction is less than zero, and the one in $z$-direction is larger than zero because the upper blade is subjected to larger force due to the larger wind velocities. Similarly, at $\theta = \pi/2$, the resultant force component in the $y$-direction is less than zero again, and the one in $z$-direction is zero due to symmetry. At $\theta = 3\pi/4$, the resultant force component in $y$-direction is identical to the one at $\theta = \pi/4$, whereas the one in $z$-direction is less than zero (opposite to the case of $\theta = \pi/4$). The negative mean value of $F_y$ was reported under the wind shear inlet condition by Sezer-Uzol and Uzol.[37] However, they also reported a negative mean value of $F_z$ that was of smaller magnitude than $F_y$. The observation is different than the results determined in the present study. In case of a large two-blade wind turbine with 30 m diameter that rotates at 34.5 rpm with the same tip-speed ratio as in the present study, the average wind velocity will be 10 m s$^{-1}$. Based on the present estimation of the force coefficients, the wind turbine bears a periodic loading status, ranging from 0 to 865 N in the $y$-direction and from $-432$ to 432 N in the $z$-direction. The results indicate that the asymmetric inflow profile causes the fluctuation of the loads and more importantly generates continuous loads in the negative $y$-direction, which will result in the shortening of the fatigue life of the turbine components.

### 4.3. Characteristics of flow field near wind turbine blade

Accurate prediction of the characteristics of flow field near the turbine blades is important for designing wind turbines. The actuator disk and actuator line methods represent effective tools for optimizing energy harvest, but they fail to capture the real flow physics near the blade surface due to the underlying assumption of replacing the physical existence of rotating blades with distributed forces along a permeable disk or lines. As a result, they are unable to resolve the flow in the boundary layer where flow separation may become more pronounced and stall effects may occur to reduce lift at certain angles of attack. The insights of flow separation phenomena can be obtained by solving the filtered Navier–Stokes equations in LES, which take the viscous effect into consideration.

The present simulation results give the detailed flow structures around the blade surface. Figure 7 shows the instantaneous streamlines on the blade surfaces on both the pressure and the suction sides for the baseline case and wind shear case observed in a reference frame rotating with the blade. In addition, the two-dimensional vector field (colored by the vorticity component in the spanwise direction, $\omega_r$) at two representative sections, $r/R = 0.63$ and $r/R = 0.95$, at phase $\theta{=}\pi/2$ (blade in vertical position) is shown. For the baseline case [Figure 7(a)], the streamlines on the suction side exhibit flow separation near the trailing edge, while streamlines on the pressure side display laminar flow characteristics. These results indicate that the boundary flow is developing not only along the streamwise direction (from leading edge to trailing edge) but also along the spanwise direction (from the blade root to the tip). The separation point on the suction side moves toward the trailing edge from the blade root to the tip, i.e., the separation areas are reduced. For the results from the wind shear case [Figure 7(b), $\theta{=}\pi/2$], the top blade is in high wind, while the bottom blade is in low wind. The separation area covers almost half of the top blade surface, while the separation points on the bottom blade are close to the trailing edge.

Furthermore, the flow structures surrounding the blade surface at selected spanwise sections (Figure 7) depict the boundary layer development from the leading edge to the trailing edge. At $r/R = 0.63$, reversed flow patterns indicate flow separation, forming two separation bubbles adjacent to the trailing edge and initiating unsteady vortex shedding in the baseline case. More pronounced flow separation occurs in the wind shear case. The second trailing vortex is more obvious, which suggests much stronger vortex shedding under large wind speed. However, this flow detachment is not observed at $r/R = -0.63$ where wind speed is lower. At $r/R = 0.95$, less severe separation is present, suggesting more consistent lift generation in this region than in the near root region. The vorticity component along the spanwise direction in the rotating frame, $\omega_r$, has opposite signs at the suction side and the pressure side. A wider range of vorticity magnitude is presented at


*Wind Energ.* 2016; **19**:803–824 © 2015 John Wiley & Sons, Ltd.
DOI: 10.1002/we

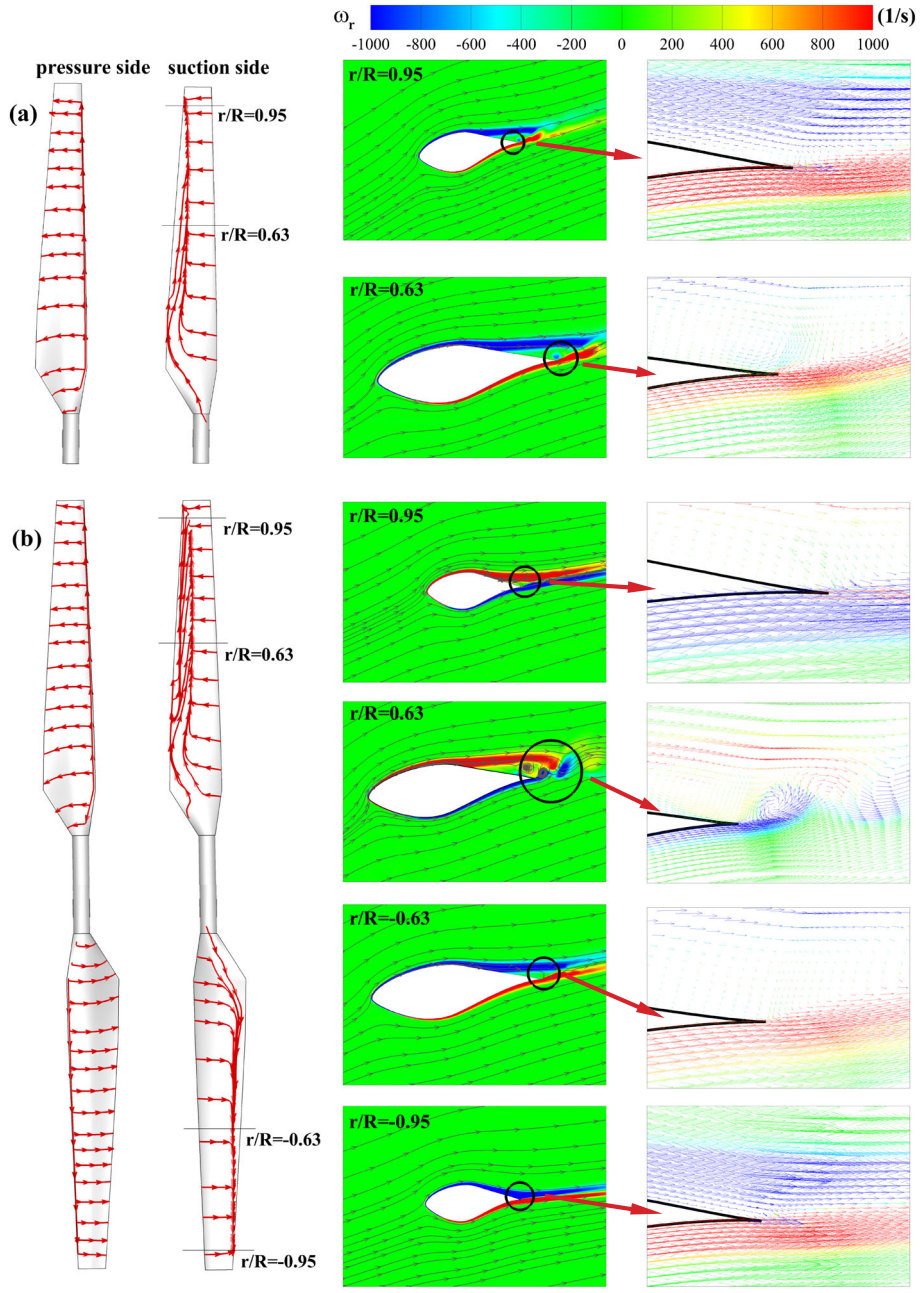


**Figure 7.** Streamlines on the pressure and suction sides of the blades and two-dimensional velocity field of flow at two representative spanwise sections when blades rotate to vertical position ($\theta=\pi/2$): (a) baseline case and (b) wind shear case. Plotted are relative velocities observed from a moving frame rotating with the blades.

$r/R = 0.63$ than at $r/R = -0.63$ in the wind shear case. After the separation point, an alternating recirculation pattern is observed. This pattern triggers a train of vortices shed from this region.

The results in Figure 7(b) reveal that uneven wind will generate different flow structures near the blade and will eventually result in uneven loading on the turbine blades, as shown in Figure 5. This uneven loading will exaggerate unstable fatigue loading on the drivetrain. This analysis will help to improve the turbine blade design and loading management by, for example, adopting blade pitch/yaw optimization, to achieve optimal balance between loading status and energy harvest.

### 4.4. Development of wake structures

The wake structures behind the wind turbine rotor are affected by the inflow conditions, and substantially influence downstream wind turbine performance. Typical instantaneous wake flow structures under three inflow conditions are visualized in Figure 8, which shows the isosurfaces of $\lambda_2$ (the negative value of the second eigenvalue of the symmetry square of velocity gradient tensor). To further visualize the development of the tip vortex, the vorticity magnitude in the central $x$-$z$-plane ($y = 0$) at two orthogonal phases, $\theta = 0$ and $\theta = \pi/2$, is shown in Figure 9. The tip vortices are initially generated because of the interactions between blade tips and their surrounding fluid as the blades are rotating, and they are stretched to form a helical path to a certain downstream distance before they are dissipated. In the baseline case, the wake structures are well-organized, periodic and symmetric. A pair of tip vortices is observed from the turbine rotor to a downstream location about $x/D = 1.3$. In the wind shear case, the tip vortex structure stays nearly intact for about four revolutions ($x/D \leq 0.7$), and the top part of the tip vortices travels faster than the bottom ones, due to the presence of wind shear, resulting in a skew structure. The disappearance of the phase-dependent (helical) vortex structure in both the baseline and wind shear cases when $x/D > 1.5$ is also apparent. Because of the shear effect between the near-blade tip vortex and the ambient flow (as discussed in Section 4.5.2), the strong vortex core in the helical structure dissipates and gradually transforms into a continuous vortex sheet, indicating the appearance of a continuous shear layer that has no phase dependence. According to similar simulations using a three-dimensional unsteady vortex-panel method in the baseline case by Sezer-Uzol and Uzol,[37] the helical structure can persist over a long downstream distance (16 revolutions and $x/D \sim 5$). The lack of turbulence production and dissipation mechanisms in that potential flow solver prevents the prediction of the detailed flow structures such as the breakdown of the tip vortices of turbine wakes, as shown in Figures 8 and 9.

In the turbulent shear case, the tip vortices are visible in the first four revolutions but are less intact than the vortices in the other two cases. Under the influence of both inflow turbulence and turbulence generated in the near wake, the wake struc-

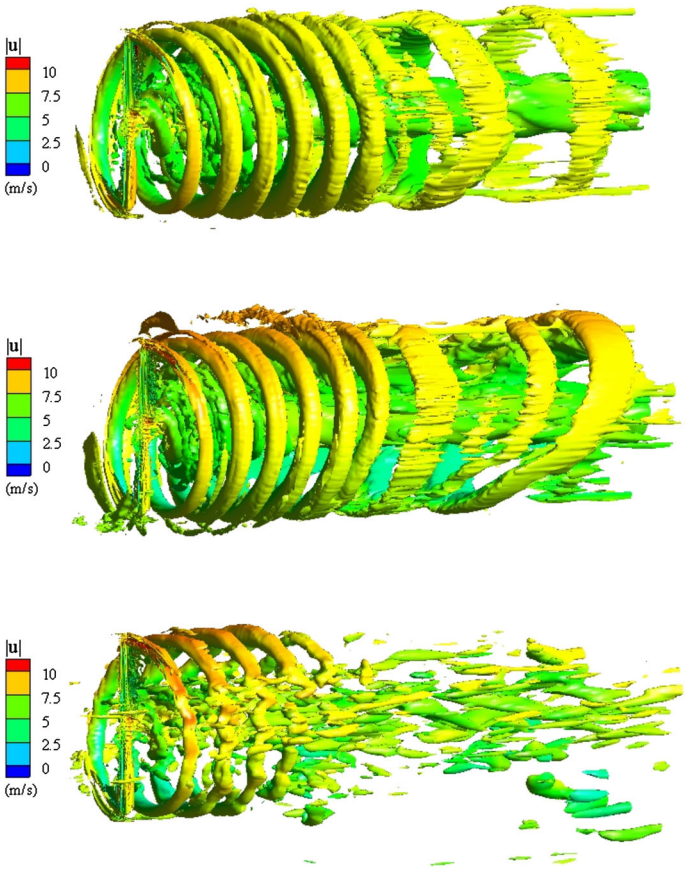


**Figure 8.** Comparison of the isosurfaces of vortex cores colored by instantaneous velocity magnitude: (top) baseline case, (middle) wind shear case and (bottom) turbulent shear case.


*Wind Energ.* 2016; **19**:803–824 © 2015 John Wiley & Sons, Ltd.
DOI: 10.1002/we

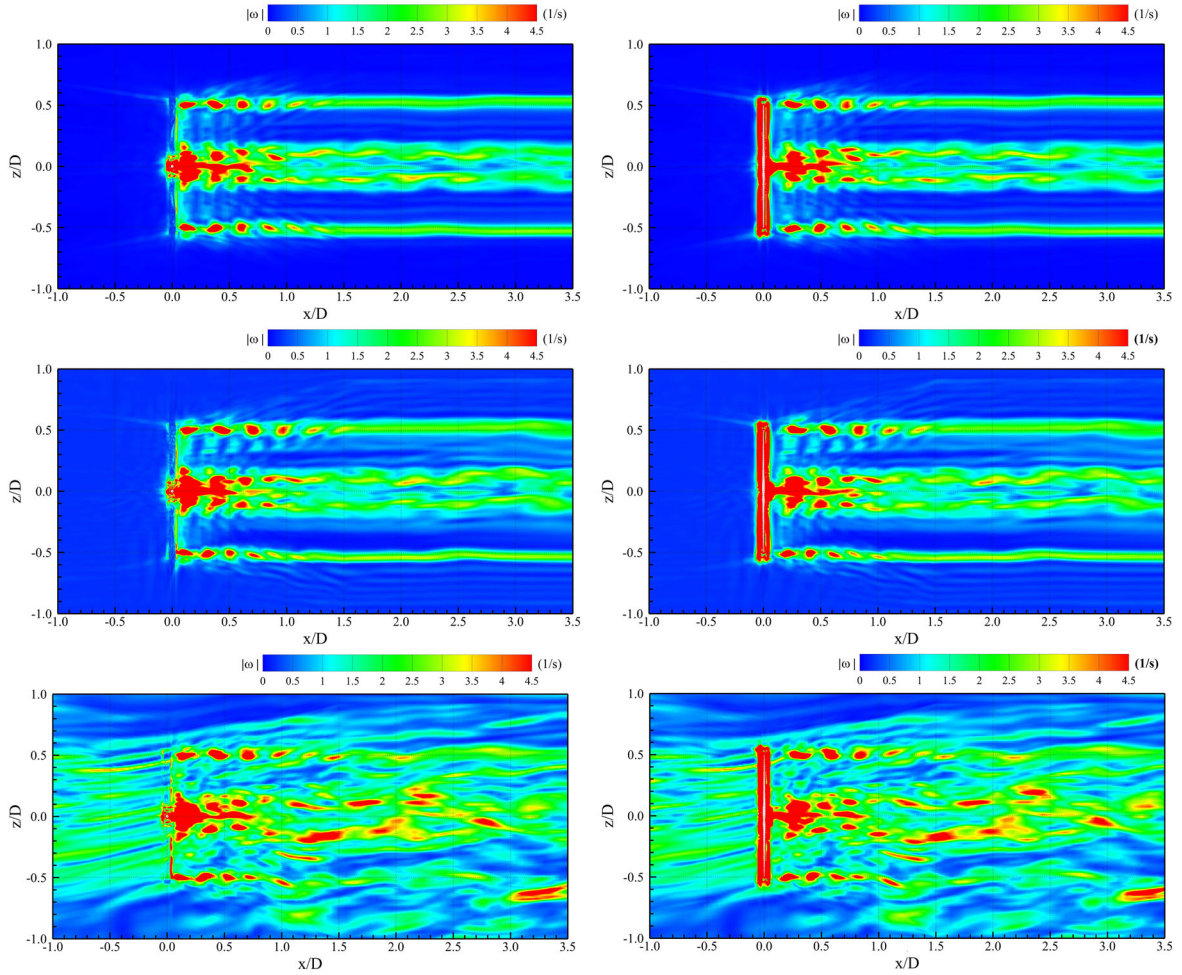


**Figure 9.** Distribution of instantaneous vorticity magnitude in the central $x$–$z$-plane: (top) baseline case, (middle) wind shear case and (bottom) turbulent shear case. Wind turbine blades are in horizontal positions ($\theta = 0$, left panel) and vertical positions ($\theta = \pi/2$, right panel).

ture quickly dissipates and displays a highly unstable nature as it travels further downstream. The observed breakdown in the pattern after four to five revolutions in the near wake is similar to what was observed in particle image velocimetry (PIV) measurements using scaled model turbine, as reported by Zhang *et al.*[15] The breakdown mechanism of the tip vortex will be discussed in Section 4.5.2. The distribution of vorticity magnitude also explains the turbulence effect in the wake pattern. The visibility of helical pattern decreases along streamwise direction, especially after $x/D = 1.2$. In Figure 9, the distributions of the vorticity magnitude at two orthogonal phases show a similar pattern, indicating the phase independence of the vorticity pattern.

In order to better identify the vortex structures in wake, the contours of normalized time-averaged streamwise vorticity, $\langle\omega_x\rangle = \frac{D}{2U_{\text{hub}}}(\frac{\partial\langle v\rangle}{\partial z} - \frac{\partial\langle w\rangle}{\partial y})$, in the $y$–$z$-plane for the three cases are plotted at three downstream locations $x/D = 1.0$, 2.0 and 3.0 in Figure 10. The vortex ring with positive vorticity is formed at the tip swept area owning to the formation of helical tip vortices. The magnitude of the $\langle\omega_x\rangle$ for the vortex ring becomes smaller with downstream distance, which can be interpreted as the dissipation of the vortices. The features of the vortex ring are identical to the wake structure shown in Figure 8.

Similar features of the vortex pattern are noticed for the wind shear case (Figure 10), but the positive large vortex rings are not as symmetric and uniform as those in the baseline case. The dissipation rate of the vortex ring is faster, and the ring becomes blurry at a distance of $x/D$=3.0. The distinct vortex patterns are found by comparing the turbulent wind shear case with the former two cases. The quick diffusion and expansion take place when $x/D > 1.0$, which causes the complete breakdown of the vortex structure, and the more scattered vorticity distribution occurs at $x/D = 2.0$ and 3.0.

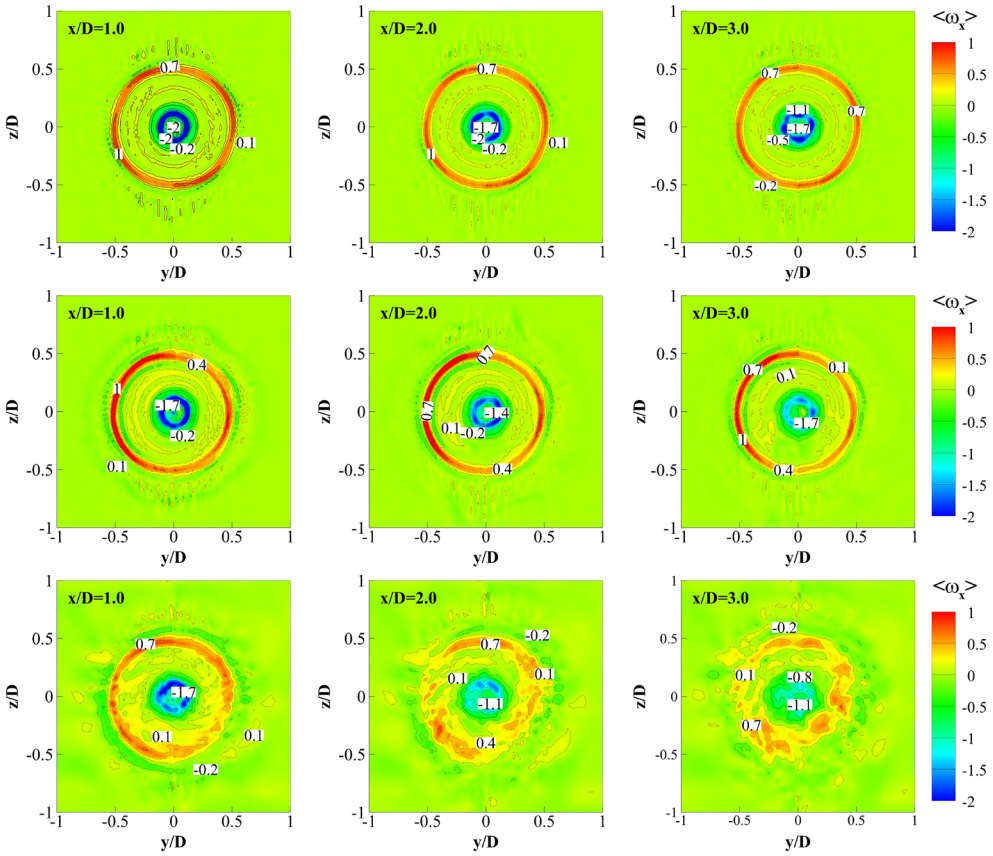


**Figure 10.** Contours of normalized time-averaged streamwise vorticity $\langle\omega_X\rangle$ in $y$–$z$-plane at downstream locations ($x/D = 1.0$, 2.0 and 3.0): (top row) baseline case, (middle row) wind shear case and (bottom row) turbulent shear case.

## 4.5. Wake characteristics

As discussed in Section 4.2, varying inflow profiles and the presence of turbulence lead to power fluctuation, unsteady loads and continuous deflection loads. Further analysis of the velocity field and the turbulence field in wake flow provides essential information for operation conditions of downstream wind turbines in a wind farm. In Section 4.5.1, the time-averaged characteristics of the three velocity components in the wake behind the wind turbine under three cases are discussed. In Section 4.5.2, turbulent kinetic energy (TKE) and turbulence production in three spatial directions are analyzed.

### 4.5.1. Mean wake profiles.

Figure 11 shows the distribution of time-averaged streamwise velocity $\langle u\rangle$ in the central $x$–$z$-plane ($y = 0$) from $x/D = -1.0$ to $x/D = 3.5$, together with the mean streamwise velocity distribution in the $y$–$z$-plane at a representative location $x/D = 2.0$. $\langle u\rangle$ displays variations in both the lateral and vertical directions for both the wind shear and turbulent shear cases due to the interaction of wind shear and rotating wake. The centers of the low velocity regions in these two cases shift to the $-y$-direction. This is because the rotating wake structure (clockwise in the right panel of Figure 11) transports momentum from the high wind part to the low wind part in the $y > 0$ region and from the low wind part to the high wind part in the $y < 0$ region. The three-dimensional structure of the wake flow is shown by the distributions of $\langle v\rangle$ and $\langle w\rangle$ in Figure 12 at $x/D = 2.0$, indicating a rotating wake induced by turbine blades. In the three cases, peak values of $\langle v\rangle$ occur in locations close to the root of each blade, e.g., for baseline case, at $(z = \pm 0.4R, y = 0)$. A similar phenomenon is observed for $\langle w\rangle$, and the peak values occur at $(y = \pm 0.4R, z = 0)$ for the baseline case.

To examine the development of the wake structure, the vertical profiles of $\langle u\rangle$, $\langle v\rangle$ and $\langle w\rangle$ at seven selected locations ($x/D = -1.0, 0.5, 1.0, 1.5, 2.0, 2.5$ and 3.0) are plotted in Figure 13. The 'W' shape profiles of $\langle u\rangle$ are observed for all three

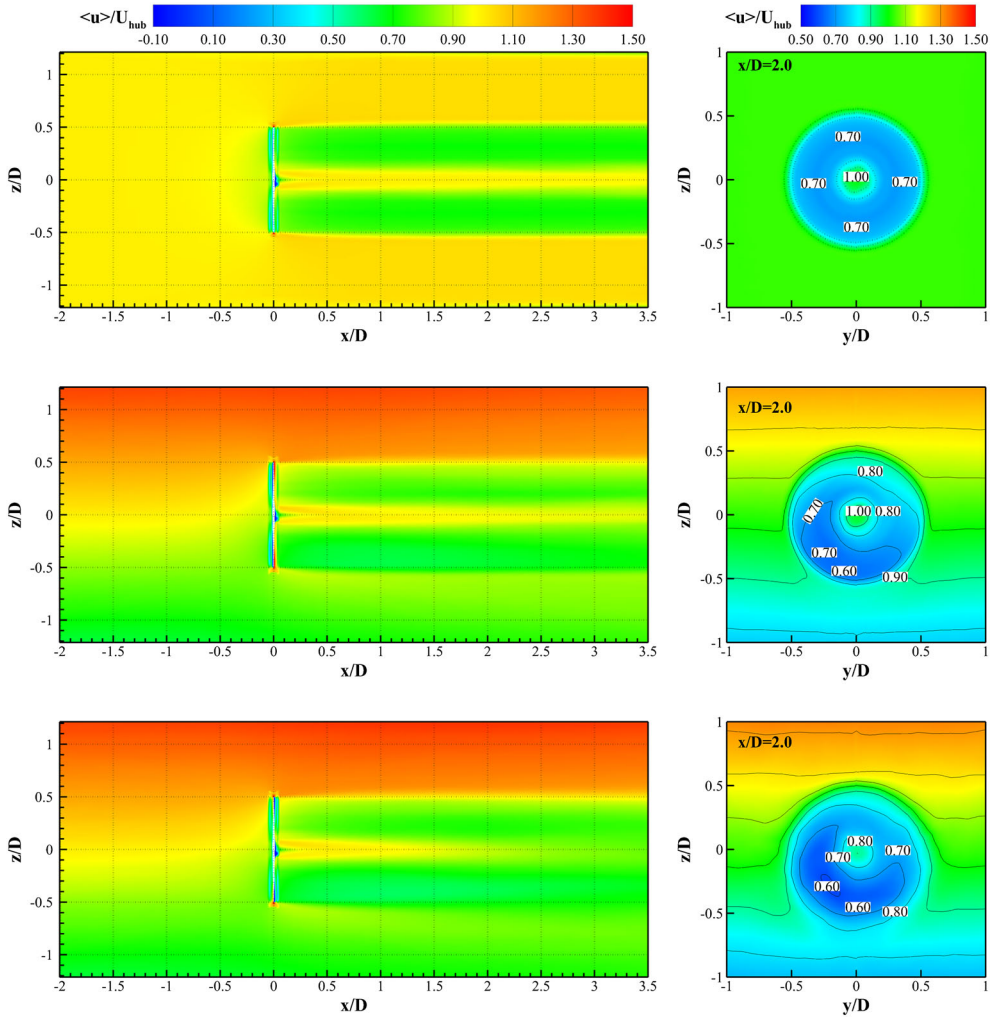


**Figure 11.** Distributions of the time-averaged streamwise velocity in the central $x$–$z$-plane (left) and $y$–$z$-plane ($x/D = 2.0$, right): (top) baseline case, (middle) wind shear case and (bottom) turbulent shear case.

cases. The baseline case results are similar to the simulation work that was reported by Mo *et al.*.[31] The profiles of $\langle u \rangle$ for the wind shear and turbulent wind shear cases are almost identical in the near wake region ($x/D \leq 1.0$). In the far wake region, the profiles of the turbulent shear case become flatter in the outer region of wake ($|z|/D \sim 0.5$), due to enhanced momentum exchange and entrainment of ambient fluid. No significant differences are observed from $z$ profiles for both $\langle v \rangle$ and $\langle w \rangle$ for the three cases. The maximum $|\langle v \rangle|$ is about 14% of $U_{\text{hub}}$ at $x/D = 1.0$.

To quantify the velocity deficit in wake, Figure 14 shows three characteristic velocities, $\langle u_c \rangle$, $\langle u_{1/4} \rangle$ and $\langle u_{-1/4} \rangle$, corresponding to center line ($z = 0$), upper half span ($z/D = 1/4$) and lower half span ($z/D = -1/4$), respectively. For the baseline case, the developments of $\langle u_c \rangle$, $\langle u_{1/4} \rangle$ and $\langle u_{-1/4} \rangle$ along the downstream show the persistent velocity deficit, i.e., no obvious wake recovery observed in the present computational domain ($0 < x/D < 3.5$). The maximum velocity deficit is about 27.5% of $U_{\text{hub}}$, occurring at half span of each blade. In both the wind shear and the turbulent shear cases, velocity recovery is observed from the development of $\langle u_{1/4} \rangle$ and $\langle u_{-1/4} \rangle$. A continuous decrease of $\langle u_c \rangle$ is observed, with maximum values of 5% and 17.5% of $U_{\text{hub}}$ at $x/D = 3.0$ for the wind shear case and turbulent shear case, respectively. The velocity recovery indicated by the increased values of $\langle u_{-1/4} \rangle$ is more obvious at the bottom region when $x/D > 0.5$. The maximum velocity deficits happen at $x/D = 1.0$, which are 24.9% and 28.3% of $U_{\text{hub}}$ for wind shear and turbulent shear cases, respectively. Slight velocity recovery is observed behind the top turbine blade in wake, and the maximum velocity deficits are 28.9% and 31.6% for the two wind shear cases.

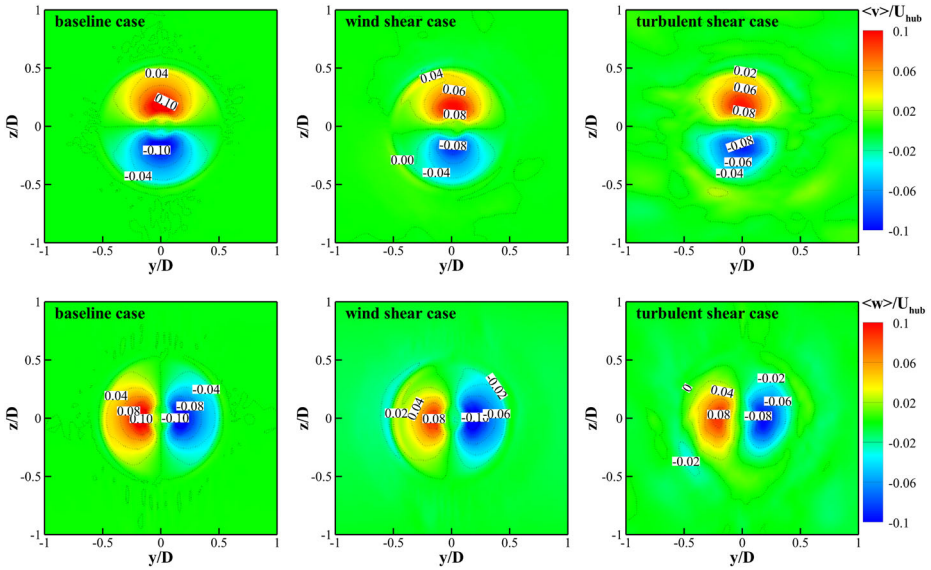


**Figure 12.** Distributions of $\langle v \rangle$ (top) and $\langle w \rangle$ (bottom) in $y$–$z$-plane at $x/D = 2.0$.

### 4.5.2. Turbulent characteristics in wake.

The spatial distribution of turbulent kinetic energy, $e \equiv \frac{1}{2}\langle u'^2 + v'^2 + w'^2 \rangle$, is shown in Figure 15. For the baseline case, in the near wake ($x/D \leq 1.0$), the maximum TKE occurs at hub height as well as at both the top tip and bottom tip regions, and the profile is almost symmetric. The maximum value of $e/{U_{\text{hub}}}^2$ is about 0.002 at $x/D = 0.5$, which diminishes downstream. When wind shear is present, the peak values of $e$ also occur at tips and hub heights in the near wake, with a maximum value of 0.008 observed at $z/D \simeq 0.45$. In the far wake, at $x/D = 3.0$, the average value of $e/{U_{\text{hub}}}^2$ within the blade swept area is approximately 0.006, which is larger than that in the near wake, indicating an increase of turbulence level due to mixing and entrainment. In the turbulent shear case, the variations of $e$ are more evident than in the wind shear case. At $x/D = 0.5$, the profile is similar to the wind shear case, and at further downstream, a strong enhancement of $e$ is noticeable. A pronounced peak of $e$ is observed at the bottom tip, which is larger than its value at the top tip in the transition region from near wake to far wake ($1.0 \leq x/D \leq 3.0$). This significant difference between the top tip and the bottom tip can be partially explained by the observed larger mean velocity gradient $\partial\langle u \rangle/\partial z$ in the bottom tip region (shown in Figure 13), which contributes to the larger turbulence production mechanism to be discussed later. Detailed examination in this transition region shows that $e$ keeps increasing at the bottom tip until reaching a maximum of 0.014 at $x/D = 2.5$, and its value increases at the top tip. Similar phenomenon has been reported in wind tunnel data in this transition region.[15,49] This trend is different than the results from several other similar simulations (e.g., previous studies[29,33]), in which the top tip region gives a larger TKE than the bottom tip region. To further investigate this discrepancy, the transport equation of $e$ for incompressible flow[50]

$$\frac{\partial e}{\partial t} + \langle u_i \rangle \frac{\partial e}{\partial x_i} = \mathcal{P} - \epsilon - \frac{\partial T_i'}{\partial x_i} \tag{17}$$

was examined. Here, $\mathcal{P} \equiv -\langle u_i' u_j' \rangle \frac{\partial \langle u_i \rangle}{\partial x_j}$ is the production term, $T_i' \equiv \frac{1}{2}\langle u_i' u_j' u_j' \rangle + \langle u_i' p' \rangle/\rho - 2\nu\langle u_j' s_{ij} \rangle$ the turbulence transport term and $\epsilon \equiv 2\nu\langle s_{ij} s_{ij} \rangle$ the dissipation term, where $s_{ij} = \frac{1}{2}(\frac{\partial u_i'}{\partial x_j} + \frac{\partial u_j'}{\partial x_i})$. $\mathcal{P}$ represents the action of the mean velocity gradients working against the Reynolds stresses to transfer kinetic energy from the mean flow to small-scale turbulence,[50] and negative values of $\mathcal{P}$ only occur in unusual situations.[51] Terms $\epsilon$ and $\partial T_i'/\partial x_i$ are usually much less than $\mathcal{P}$ so they can be neglected.[51] Thus, $\mathcal{P}$ makes the major contribution to the turbulence production mechanism.

In the present study, the production is evaluated using LES results. Similar to the discovery by Wu and Porté-Agel,[46] the total production is mainly contributed by two components: $\mathcal{P}_{uv} = -[\langle \tilde{u}'\tilde{v}' \rangle + \langle \tau_{uv} \rangle]\frac{\partial \langle u \rangle}{\partial y}$, and $\mathcal{P}_{uw} = -[\langle \tilde{u}'\tilde{w}' \rangle + \langle \tau_{uw} \rangle]\frac{\partial \langle u \rangle}{\partial z}$. Recall that $\tau_{ij}$ is the SGS stress. It is further identified that $\langle \tau_{ij} \rangle \ll \langle \tilde{u}_i' \tilde{u}_j' \rangle$, so the contribution of SGS stresses can be ignored, i.e., $\langle u_i' u_j' \rangle \simeq \langle \tilde{u}_i' \tilde{u}_j' \rangle$ and $\frac{\partial \langle u_i \rangle}{\partial x_j} \simeq \frac{\partial \langle \tilde{u}_i \rangle}{\partial x_j}$. With these simplifications, the production is estimated by

$$\mathcal{P} \simeq -\langle \tilde{u}'\tilde{v}' \rangle \frac{\partial \langle \tilde{u} \rangle}{\partial y} - \langle \tilde{u}'\tilde{w}' \rangle \frac{\partial \langle \tilde{u} \rangle}{\partial z}. \tag{18}$$

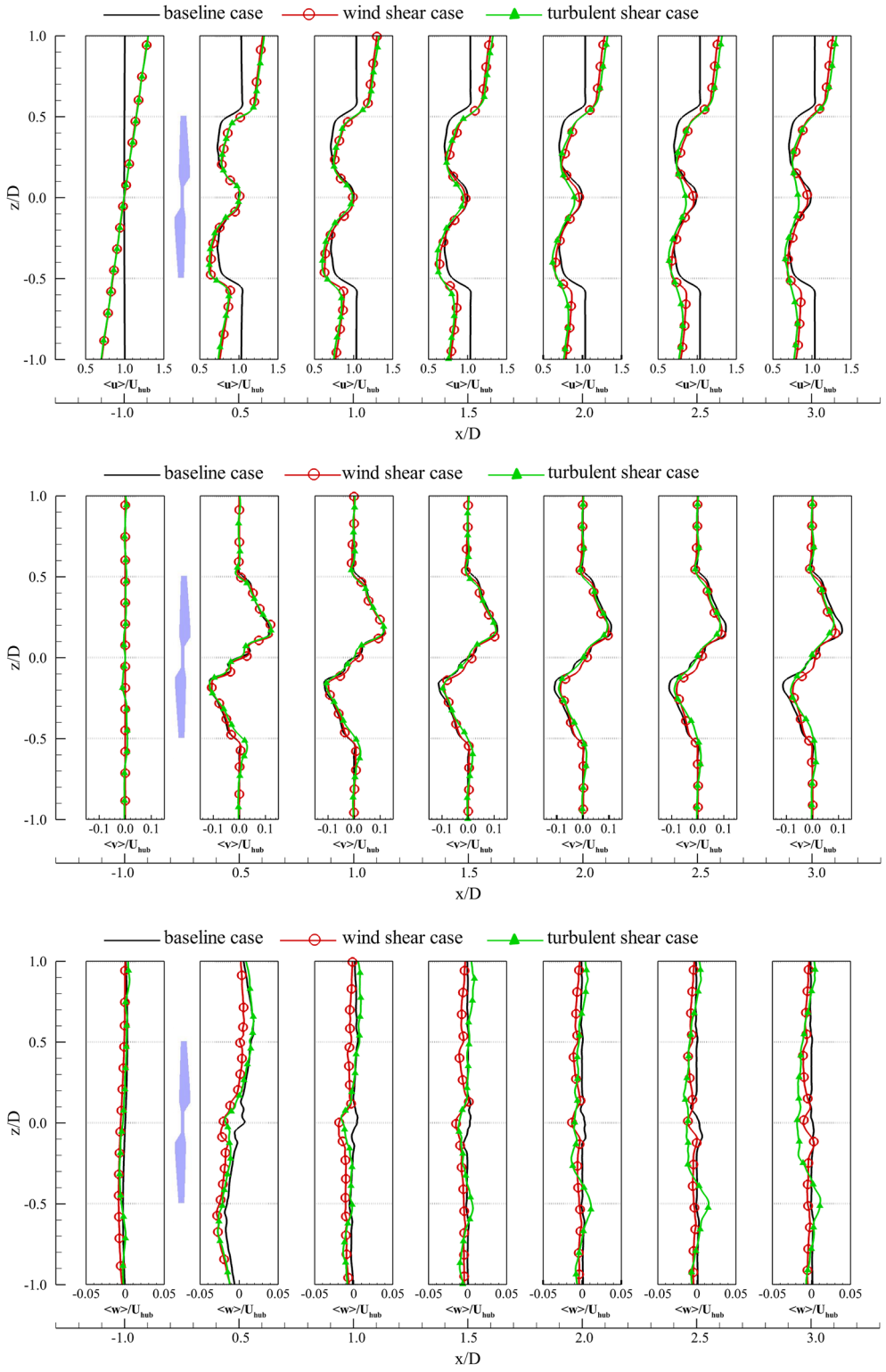


**Figure 13.** *z*-Profiles of time-averaged velocity components at selected downstream locations: (top) $\langle u \rangle$, (middle) $\langle v \rangle$ and (bottom) $\langle w \rangle$.

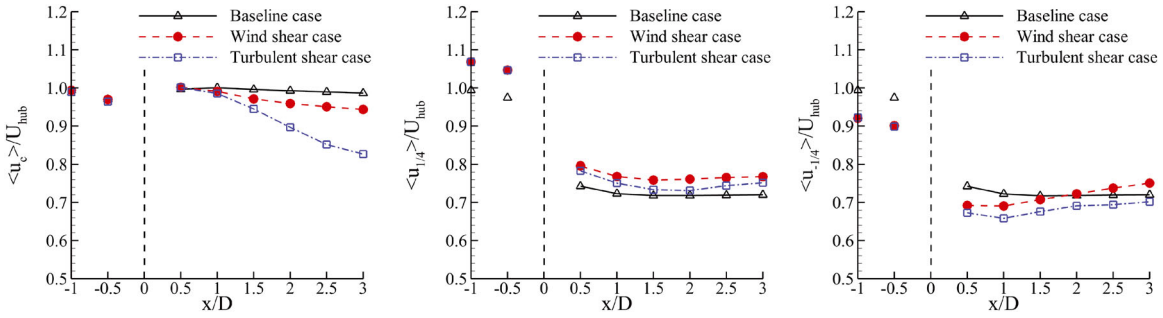


**Figure 14.** Development of the time-averaged streamwise velocity at different downstream locations: (left) center line $z/D = 0$, (middle) upper half span $z/D = 1/4$ and (right) lower half span $z/D = -1/4$. Vertical dashed line indicates the location of wind turbine.

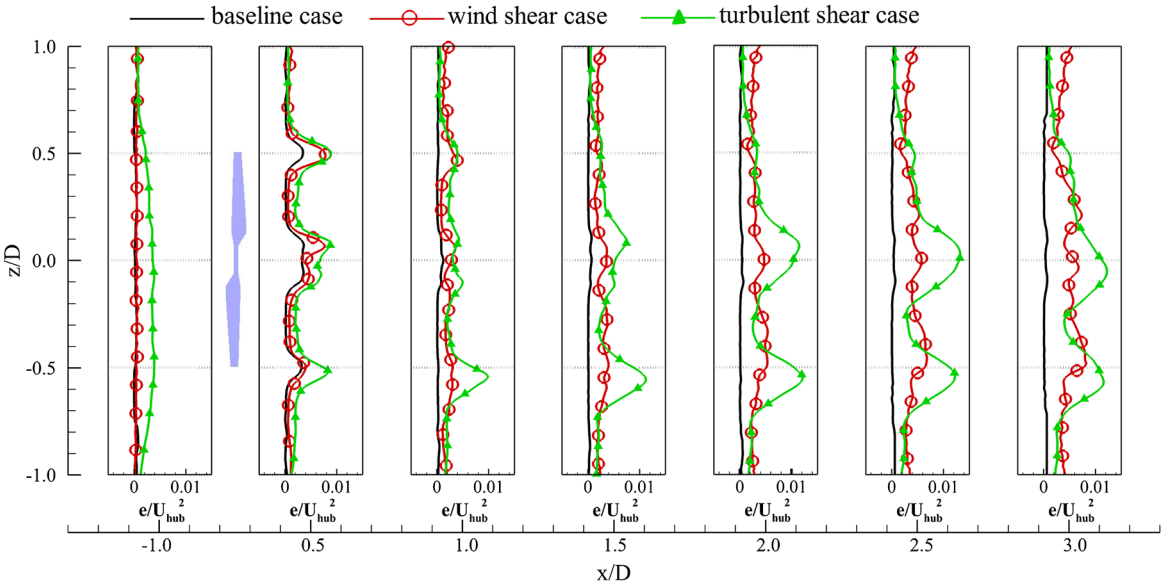


**Figure 15.** $z$-Profiles of $e$ at selected downstream locations.

The distributions of $\mathcal{P}$ at representative locations of $x/D = 1.0$ and 3.0 are compared in Figure 16 for the baseline case and turbulent shear case. It is evident in the tip swept area that the $\mathcal{P}$ for both cases is significantly larger than that in other regions of the wake at $x/D = 1.0$. Even in the baseline case, where the inflow is uniform and least turbulent, energy is extracted from the large structure in the tip swept area, where the tip vortex is formed and a large velocity gradient exists, and fed into small turbulence structures. In the turbulent shear case, where the magnitudes of the velocity gradients and turbulent levels are significantly increased, escalated turbulence production explains the earlier breakdown of tip vortex, and the appearance of small turbulent patches sheds into the far wake as observed in Figures 8 and 9. In the turbulent shear case, $\mathcal{P}$ at the bottom tip is higher than the top tip within the near wake (e.g., $x/D = 1.0$), but the trend is reversed in the far wake at $x/D = 3.0$. The plots of $\mathcal{P}$ in Figure 16 show that the value of $\mathcal{P}$ at the top tip continues to increase as $x$ increases. However, $\mathcal{P}$ keeps decreasing at the bottom tip due to the decreased $\frac{\partial \langle u \rangle}{\partial z}$, indicating expansion and weakening of the shear layer zone observed in Figure 13 along the downstream direction. This explains the peak of $e$ at the bottom tip in Figure 15, which continues to amplify downstream. In the present domain, although $e$ is larger at the bottom tip, it is expected that at a point far enough downstream, $e$ at the top tip will be larger since the $\mathcal{P}$ at the top tip is significantly larger. Since in the present study the turbine tower and nacelle are omitted, the analysis of turbulent generation mechanism is simplified in the near wake. More systematic analysis is needed with more realistic simulation results to capture this interaction.


*Wind Energ.* 2016; **19**:803–824 © 2015 John Wiley & Sons, Ltd.
DOI: 10.1002/we

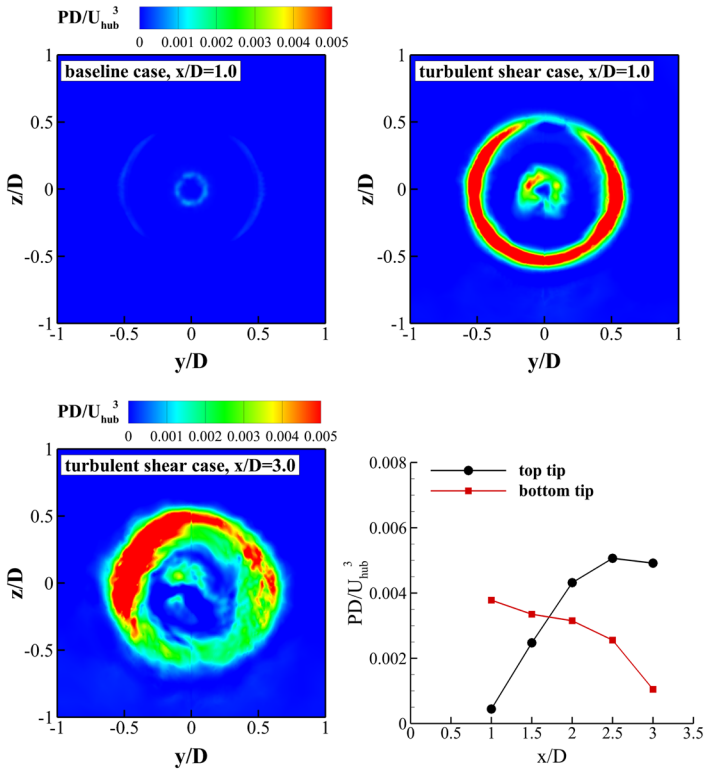


**Figure 16.** Contour plots of turbulence production for both the baseline case ($x/D = 1.0$) and the turbulent shear case ($x/D = 1.0$ and 3.0). Line plots of $\mathcal{P}$ are also shown at the top and bottom tips of the turbulent shear case.

## 5. CONCLUSION

This paper presents LESs of flow fields around a 10 m diameter NREL phase VI wind turbine using the exact blade geometry. The methodology is capable of resolving details of near-blade flow in turbulent wind, where viscous effects must be considered, and predicting directly the unsteady turbine loading at different rotation phases. These details cannot be predicted accurately by other methods employing simplified treatments for the blade geometries. Three different inflow conditions are studied as follows: baseline case with a uniform wind profile, a wind shear case and a turbulent wind shear case. The simulation of the baseline case is carried out under the identical boundary conditions as in the wind tunnel experiments for simulation validation. The simulation results for the blade profile pressure coefficient distributions accurately match the experimental measurements. Quantitative comparisons of the three cases lead to insight into the influence of the inflow conditions, with the following key discoveries.

- The presence of wind shear induces periodic variations and fluctuations in the power output and aerodynamic loading applied on the wind turbine, which represent the fatigue loading on the drivetrain. More importantly, such wind variations induce a continuous DC loading in the lateral ($y$) direction. The flow separates on the suction side of blade surface. In the separation zone, spanwise motion is also present. More pronounced flow separation on the suction side occurs in the high wind region than in the low wind region.
- The wind shear and turbulence effects destroy the uniform and symmetric wake structure in the far wake. Because of the shear between the near-blade tip vortex and the ambient flow, the evident helical structure gradually transforms to a continuous vorticity sheet when $x/D > 1.5$, indicating the existence of a continuous shear layer that has weak phase dependence. The tip vortex breakdown pattern is observed after four to five revolutions.
- The wake region is characterized by the existence of strong three-dimensionality. The other two velocity components are about 14% of the streamwise component. The presence of wind shear changes the distribution of streamwise velocity, but does not significantly change the lateral and vertical velocity distributions.
- The TKE in the wake of the turbulent shear case is much larger than that of the baseline case. The turbulence production is significantly larger in the tip swept area due to high velocity gradients and turbulence levels, and serves as a mechanism for the breakdown of the tip vortex in the near wake. In the near wake, the production is higher at

the bottom tip than at the top tip, and the trend is reversed in the far wake. This explains the appearance of a peak TKE at the bottom tip in the present simulation domain. TKE is expected to be larger at the top tip at distances far enough downstream.

Quantitative analysis of the effect of inflow conditions on wind turbines is of significance not only to wind turbine design but also to wind farm control. In particular, accurate predictions of turbine response to varying inflow wind will lay the foundation for developing realistic aerodynamic models that will enable the long-term healthy operation of wind farms with optimal energy harvest by wind turbine clusters and alleviated maintenance costs. Future research will investigate the effects of varying tip-speed ratio and wind speed. In addition, including the nacelle and tower geometry in the model will lead to more accurate wake profiles. Furthermore, the ABL profile is important.[52] The simulation results will provide valuable information for the wind energy community by adopting more realistic ABL profiles and turbulence characteristics. Investigations of far wake characteristics should also be carried out to develop low-order wake models.

## REFERENCES


1. Leung DY, Yang Y. Wind energy development and its environmental impact: a review. *Renewable and Sustainable Energy Reviews* 2012; **16**: 1031–1039.
2. Deal WF. Wind power: an emerging energy resource. *Technology and Engineering Teacher* 2010; **70**: 9–15.
3. Newstadter H, Spera D. Method for evaluating wind turbine wake effects on wind farm performance. *Journal of Solar Energy Engineering* 1985; **107**: 240– 243.
4. Barthelmie RJ, Rathmann O, Frandsen ST, Hansen K, Politis E, Prospathopoulos J, Rados K, Cabezon D, Schlez W, Phillips J, Neubert A, Schepers JG, van der Pijl SP. Modelling and measurements of wakes in large wind farms. In *Journal of Physics: Conference Series* Vol. 75, 2007; 012049.
5. Sanderse B, Aerodynamics of wind turbine wakes. *Tech. Rep*, Energy Research Center of the Netherlands (ECN), ECN-E–09-016, Petten, The Netherlands, 2009.
6. Vermeer L, Sørensen JN, Crespo A. Wind turbine wake aerodynamics. *Progress in Aerospace Sciences* 2003; **39**: 467–510.
7. Vermeer NJ, van Bussel GJW. Velocity measurements in the near wake of a model rotor and comparison with theoretical results. *Fifteenth European Rotorcraft Forum*, Amsterdam, The Netherlands, 1989; 20/1– 20/14.
8. Shimizu Y, Kamada Y. Studies on a horizontal axis wind turbine with passive pitch-flap mechanism (performance and flow analysis around wind turbine). *Journal of Fluids Engineering* 2001; **123**: 516–522.
9. Medici D, Alfredsson P. Measurements on a wind turbine wake: 3D effects and bluff body vortex shedding. *Wind Energy* 2006; **9**: 219–236.
10. Whale J, Anderson C, Bareiss R, Wagner S. An experimental and numerical study of the vortex structure in the wake of a wind turbine. *Journal of Wind Engineering and Industrial Aerodynamics* 2000; **84**: 1–21.
11. Grant I, Parkin P. A DPIV study of the trailing vortex elements from the blades of a horizontal axis wind turbine in yaw. *Experiments in Fluids* 2000; **28**: 368–376.
12. Chamorro LP, Porté-Agel F. Turbulent flow inside and above a wind farm: a wind-tunnel study. *Energies* 2011; **4**: 1916–1936.
13. España G, Aubrun S, Loyer S, Devinant P. Spatial study of the wake meandering using modelled wind turbines in a wind tunnel. *Wind Energy* 2011; **14**: 923–937.
14. España G, Aubrun S, Loyer S, Devinant P. Wind tunnel study of the wake meandering downstream of a modelled wind turbine as an effect of large scale turbulent eddies. *Journal of Wind Engineering and Industrial Aerodynamics* 2012; **101**: 24–33.
15. Zhang W, Markfort CD, Porté-Agel F. Near-wake flow structure downwind of a wind turbine in a turbulent boundary layer. *Experiments in Fluids* 2012; **52**: 1219–1235.
16. Xu G, Sankar LN. Computational study of horizontal axis wind turbines. *Journal of Solar Energy Engineering* 2000; **122**: 35–39.
17. Sørensen JN, Shen WZ. Numerical modeling of wind turbine wakes. *Journal of Fluids Engineering* 2002; **124**: 393–399.
18. Sørensen NN, Michelsen J, Schreck S. Navier–Stokes predictions of the NREL phase VI rotor in the NASA Ames 80 ft× 120 ft wind tunnel. *Wind Energy* 2002; **5**: 151–169.
19. Gómez-Iradi S, Barakos G. Computational fluid dynamics investigation of some wind turbine rotor design parameters. *Proceedings of the Institution of Mechanical Engineers, Part A: Journal of Power and Energy* 2008; **222**: 455–470.

20. Potsdam MA, Mavriplis DJ. Unstructured mesh CFD aerodynamic analysis of the NREL phase VI rotor. *47th AIAA Aerospace Sciences Meeting including the New Horizons Forum and aerospace exposition*, Orlando, Florida, 2009; AIAA 2009–1221.
21. Mo JO, Lee YH. CFD investigation on the aerodynamic characteristics of a small-sized wind turbine of NREL phase VI operating with a stall-regulated method. *Journal of Mechanical Science and Technology* 2012; **26**: 81–92.
22. Moshfeghi M, Song YJ, Xie YH. Effects of near-wall grid spacing on SST-K-$\omega$ model using NREL phase VI horizontal axis wind turbine. *Journal of Wind Engineering and Industrial Aerodynamics* 2012; **107**: 94–105.
23. Sanderse B, Pijl S, Koren B. Review of computational fluid dynamics for wind turbine wake aerodynamics. *Wind Energy* 2011; **14**: 799–819.
24. Stovall T, Pawlas G, Moriarty P. Wind farm wake simulations in OpenFoam. *48th AIAA Aerospace Sciences Meeting Including the New Horizons Forum and Aerospace Exposition*, Orlando, Florida, 2010; AIAA 2010-825.
25. Jimenez A, Crespo A, Migoya E, Garcia J. Advances in large-eddy simulation of a wind turbine wake. In *Journal of Physics: Conference Series* Vol. 75, 2007; 012041.
26. Jimenez A, Crespo A, Migoya E, Garcia J. Large-eddy simulation of spectral coherence in a wind turbine wake. *Environmental Research Letters* 2008; **3**: 015004.
27. Jimenez A, Crespo A, Migoya E. Application of a LES technique to characterize the wake deflection of a wind turbine in yaw. *Wind Energy* 2010; **13**: 559–572.
28. Troldborg N, Sorensen JN, Mikkelsen R. Numerical simulations of wake characteristics of a wind turbine in uniform inflow. *Wind Energy* 2010; **13**: 86–99.
29. Porté-Agel F, Wu YT, Lu H, Conzemius RJ. Large-eddy simulation of atmospheric boundary layer flow through wind turbines and wind farms. *Journal of Wind Engineering and Industrial Aerodynamics* 2011; **99**: 154–168.
30. Lu H, Porté-Agel F. Large-eddy simulation of a very large wind farm in a stable atmospheric boundary layer. *Physics of Fluids* 2011; **23**: 065101.
31. Mo JO, Choudhry A, Arjomandi M, Lee YH. Large eddy simulation of the wind turbine wake characteristics in the numerical wind tunnel model. *Journal of Wind Engineering and Industrial Aerodynamics* 2013; **112**: 11–24.
32. Ivanell S, Sørensen JN, Henningson D. Numerical Computations of Wind Turbine Wakes. In *Wind Energy*. Springer: Berlin, 2007; 259–263.
33. Wu YT, Porté-Agel F. Large-eddy simulation of wind-turbine wakes: evaluation of turbine parametrisations. *Boundary-Layer Meteorology* 2011; **138**: 345–366.
34. Porté-Agel F, Lu H, Wu YT. A large-eddy simulation framework for wind energy applications. *Fifth International Symposium on Computational Wind Engineering*, Chapel Hill, North Carolina, 2010.
35. Troldborg N, Sørensen JN, Mikkelsen R. Actuator line simulation of wake of wind turbine operating in turbulent inflow. In *Journal of Physics: Conference Series* Vol. 75, 2007; 012063.
36. Troldborg N, Larsen GC, Madsen HA, Hansen KS, Sørensen JN, Mikkelsen R. Numerical simulations of wake interaction between two wind turbines at various inflow conditions. *Wind Energy* 2011; **14**: 859–876.
37. Sezer-Uzol N, Uzol O. Effect of steady and transient wind shear on the wake structure and performance of a horizontal axis wind turbine rotor. *Wind Energy* 2013; **16**: 1–17.
38. Smagorinsky J. General circulation experiments with the primitive equations: I. The basic experiment*. *Monthly Weather Review* 1963; **91**: 99–164.
39. Wu P. Large eddy simulation of high reynolds number wall-bounded flows. *Ph.D. Thesis*, Katholieke Universiteit Leuven, 2012.
40. Hand MM, Simms D, Fingersh L, Jager D, Cotrell J, Schreck S, Larwood S. Unsteady aerodynamics experiment phase VI: wind tunnel test configuration and available data campaigns. National Renewable Energy Laboratory, 2001.
41. Simms DA, Schreck S, Hand M, Fingersh L. NREL unsteady aerodynamics experiment in the NASA-Ames wind tunnel: a comparison of predictions to measurements. National Renewable Energy Laboratory, Colorado, USA, 2001.
42. Werner H, Wengle H. Large-eddy simulation of turbulent flow over and around a cube in a plate channel. In *Turbulent Shear Flows 8*. Springer: Berlin, 1993; 155–168.
43. Paul G. *Wind Power: Renewable Energy for Home, Farm, and Business*. Chelsea Green: New York, 2004.
44. Kraichnan RH. Diffusion by a random velocity field. *Physics of Fluids* 1970; **13**: 22–31.
45. Smirnov A, Shi S, Celik I. Random flow generation technique for large eddy simulations and particle-dynamics modeling. *Journal of Fluids Engineering* 2001; **123**: 359–371.
46. Wu YT, Porté-Agel F. Atmospheric turbulence effects on wind-turbine wakes: an LES study. *Energies* 2012; **5**: 5340–5362.

47. Christakos K, Reuder J, Furevik BR. Experimental characterization of the marine atmospheric boundary layer in the Havsul area, Norway. *Energy Procedia* 2013; **35**: 121–127.
48. Burton T, Jenkins N, Sharpe D, Bossanyi E. *Wind Energy Handbook*. John Wiley & Sons: Chichester, 2011.
49. Hu H, Yang Z, Sarkar P. Dynamic wind loads and wake characteristics of a wind turbine model in an atmospheric boundary layer wind. *Experiments in Fluids* 2012; **52**: 1277–1294.
50. Pope S. *Turbulent Flows*. Cambridge University Press: UK, 2000.
51. Tennekes H, Lumley JL. *A First Course in Turbulence*. MIT Press: Cambridge, US, 1972.
52. Chamorro LP, Porté-Agel F. A wind-tunnel investigation of wind-turbine wakes: boundary-layer turbulence effects. *Boundary-Layer Meteorology* 2009; **132**: 129–149.



*Wind Energ.* 2016; **19**:803–824 © 2015 John Wiley & Sons, Ltd.
DOI: 10.1002/we